Digital twin of wind farms via physics-informed deep learning

Jincheng Zhang, Xiaowei Zhao *

Intelligent Control & Smart Energy (ICSE) Research Group, School of Engineering, University of Warwick, Coventry, UK

ARTICLE INFO

ABSTRACT

The spatiotemporal flow field in a wind farm determines the wind turbines' energy production and structural fatigue. However, it is not obtainable by the current measurement, modeling, and prediction tools in wind industry. Here we propose a novel data and knowledge fusion approach to create the first digital twin for onshore/offshore wind farm flow system, which can predict the in situ spatiotemporal wind field covering the entire wind farm. The digital twin is developed by integrating the Lidar measurements, the Navier–Stokes equations, and the turbine modeling using actuator disk method, via physics-informed neural networks. The design enables the seamless integration of Lidar measurements and turbine operating data for real-time flow characterization, and the fusion of flow physics for retrieving unmeasured wind field information. It thus addresses the limitations of existing wind prediction approaches based on supervised machine learning, which cannot achieve such prediction because the training targets are not available. Case studies of a wind farm under typical operating scenarios (i.e. a greedy case, a wake-steering case, and a partially-operating case) are carried out using high-fidelity numerical experiments, and the results show that the developed digital twin achieves very accurate mirroring of the physical wind farm, capturing detailed flow features such as wake interaction and wake meandering. The prediction error for the flow fields, on average, is just 4.7% of the value range. With the accurate flow field information predicted, the digital twin is expected to enable brand new research across wind farm lifecycle including monitoring, control, and load assessment.

1. Introduction

Wind power plays a key role in the global shift to clean growth. The global wind power installation has surpassed 837 GW at the end of 2021, while sustained and accelerated growth of wind power, especially offshore wind power, is expected in the coming decades [1]. On the other hand, the recent development of sensors, heterogeneous computing, artificial intelligence (AI), and cloud technology brings vital opportunities for the digital revolution of wind industry in the era of Industry 4.0. Digital twin (DT) [2], the digital mirroring of the physical system in the virtual space, has seen great successes in other physical and engineering systems [3], such as aviation [4], manufacturing [5], and energy [6]. It is also of great interest to wind industry. A wind farm DT, which can provide the digital mirroring of the real-time spatiotemporal wind field covering the entire wind energy site during the whole lifecycle of wind farm, can bring brand new opportunities for all the stages of wind farm development, including wind assessment [7–9], planning [10], turbine-level control [11,12], farm-level control [13–16], maintenance [17,18], repowering [19], and grid integration [20].

The key areas that will benefit from the creation of a wind farm flow DT include: (1) Wind resource assessment. The uncertainty of the intermittent wind poses great challenges in assessing the potential of a wind energy site e.g. the annual power production, the operation and maintenance (O&M) costs, and the turbine lifespan. The accurate assessment of wind resource [7–9] has a great impact on the decision-making process of wind energy planning and construction. (2) Wind turbine & farm control. The wind velocity field in real-world wind farms is chaotic and shows strong spatiotemporal variability, and the wind turbine wake effects have a great impact on the overall power production of a wind plant [13,14] and also the performance of the neighboring farms [10,19]. The accurate quantification of the spatiotemporal wind field information (including both the freestream turbulent flows and the wake flows) is therefore of great importance for the control of wind turbines [11,12] and wind farms [15,16], to increase the energy capture efficiency and mitigate the structural load. (3) Wind energy site monitoring. The real-time monitoring of wind farms is crucial for the prevention of extreme events, the reduction of structural failures, and the scheduling of turbine maintenance [17,18]. (4) Wind speed prediction. The accurate prediction of wind speed [21,22], thus wind power via power curves, is important in assisting grid integration [20], to stabilize the electricity grid and increase its resilience. All these areas require the accurate characterization, quantification, and understanding of the underlying flow system i.e. the spatiotemporal wind flows in

---

* Corresponding author.

E-mail addresses: jincheng.zhang.1@warwick.ac.uk (J. Zhang), xiaowei.zhao@warwick.ac.uk (X. Zhao).

Nomenclature

Abbreviations

AI	Artificial Intelligence
CFD	Computational Fluid Dynamics
DL	Deep Learning
DT	Digital Twin
LES	Large Eddy Simulation
Lidar	Light detection and ranging
LoS	Line-of-Sight
ML	Machine Learning
MSE	Mean Squared Error
NN	Neural Network
NREL	National Renewable Energy Laboratory
NS	Navier–Stokes
O&M	Operation and Maintenance
PIV	Particle Image Velocimetry
RANS	Reynolds-Averaged Navier–Stokes
RMSE	Root Mean Square Error
SCADA	Supervisory Control and Data Acquisition
SCRTP	Scientific Computing Research Technology Platform
SOWFA	Simulator fOr Wind Farm Applications

Symbols

D	The turbine rotor diameter
d^{μ}	The data point measured by Lidar
e_{div}	The loss term derived by the continuity equation
e_u	The loss term derived by the x momentum equation
e_v	The loss term derived by the y momentum equation
$\tilde{e}_u$	The loss term derived by the x momentum equation with the actuator force term
$\tilde{e}_v$	The loss term derived by the y momentum equation with the actuator force term
f	The actuator force
L	The total loss
L_{Lidar}	The loss derived from the Lidar module
L_{NS}	The loss derived from the NS module
L_{Turb}	The loss derived from the turbine module
$\mathcal{N}$	The deep neural network model
N_{ad}	The number of elements in the actuator disk
N_{ns}	The number of test points fed into the NS module
N_{Turb}	The number of test points fed into the turbine module
N_Y	The number of points for calculating effective wind speed
N_{μ}	The number of Lidar data points
p	The static pressure
u	The streamwise wind speed
U_{eff}	The effective wind speed
v	The spanwise wind speed
W	The trainable weights
γ	The turbine yaw angle
ϵ	The smoothing parameter of the Gaussian kernel
θ	The Lidar beam's azimuthal angle

to bring the next technological breakthroughs in these fields. It becomes even more crucial with the current trend in moving towards larger turbine rotors, where the wind varies more significantly in the whole rotor swept area, and towards deeper water sites, where the wind becomes more volatile and shows stronger spatiotemporal variability. Therefore, this work aims to develop a wind farm DT system, i.e. a model that can predict the in situ spatiotemporal wind flows across the whole wind energy site based on real-time measurements and flow physics.

The main challenge in establishing such a DT for wind farm flow system lies in, on the one hand, the lack of experimental techniques for measuring the real-time wind field covering the entire utility-scale wind farm site, and on the other hand, the complexity of the underlying physical system, i.e. the multiple scales in space and time, the strong nonlinearity, and the large degrees of freedom. The flow field measurements for wind farm wakes, both in scaled wind tunnel experiments and in utility-scale real-world wind energy sites, have been under intense investigations for many years [23,24]. For wind tunnel experiments, detailed measurements can be carried out using particle image velocimetry (PIV) equipment under controlled inflows [25]. They are of great value for the understanding of wind farm flow physics and the validations of wind farm models and control approaches. However, they cannot reflect the real-time flow fields in real-world conditions quantitatively. Moreover, the scaling issues for tunnel experiments also pose great challenges for comparison with full-scale wind farm flows. To provide full-scale measurements of utility-scale wind farms, numerous measurement campaigns have been carried out in the past. Earlier works mainly rely on the SCADA system for inflow and wake measurements [26,27]. Such measurements can last for a long time period (e.g. a few months or years). However, in terms of data types, the SCADA system can only provide point characterization at the installed locations but not the field characterization covering the spatial domain. Recently, with the advancements of remote sensing technologies, wind Lidars [28,29] were deployed in more and more measurement campaigns, aiming at providing up-to-date flow measurements for modeling and control communities. For example, in [30], Lidar measurements at various atmospheric conditions and wind directions were carried out at a wind farm site in North Texas. Along with the SCADA data, the wake-induced power losses were investigated in detail. In [31], measurement campaign at a complex terrain wind farm was carried out using two wind Lidars and the SCADA system. Then the measurement data was used for analyzing both wake and terrain effects. In [32], Lidar measurements of wind turbine wakes were obtained using the Windscanner system [33] and the Lidar data was then used to verify wake boundary identification approaches. Although Lidars can measure flow information that is spatially richer than the SCADA system, only scattered, sparse measurements can be obtained at one time instant. The field characterization was thus only obtained via averaging over the time period with the assumption of static flows in these studies. The unsteady flow characteristics were therefore lost in the averaging process. In summary, with current experimental techniques, the full spatiotemporal flow field at utility scale cannot be obtained via direct measurement.

As for the current wind modeling and prediction approaches, including the numerical, analytical, and big data-driven approaches, they

the whole wind energy site. However, what is happening in real-world scenarios remains largely unknown with the current technologies. This lack of spatiotemporal wind information needs urgent remedies in order

cannot achieve the prediction of the in situ spatiotemporal flow fields for wind farms either, as described below.

(1) Numerical approaches, including Reynolds-averaged Navier–Stokes (RANS) and large eddy simulations (LES), have been developed in the literature [34] to simulate the wakes generated by wind turbines [35,36]. However, these approaches, on the one hand, are computationally expensive where the latest developments are moving towards using exascale computing resources [37], and on the other hand, aim at the standalone simulations of fluid systems without the time-dependant scattered information from real-world sensors as input. Therefore, with these approaches, the real-time correspondence between the simulated and the real-world wind farm flow fields cannot be established.

(2) Analytical approaches [38] have also been developed with the understanding of the flow phenomena as the basis. However, these models [39–41] are of low fidelity, i.e. they are designed to capture the overall flow features and only a small number of degrees of freedom can be calibrated against real-world conditions. Thus they cannot capture the detailed spatiotemporal flow features. In [42], a comprehensive evaluation of nine analytical wake models was carried out and the results showed that there were clear discrepancies between the predicted wake effects and the reference data. Their low fidelity thus makes them not suitable for the purpose of establishing DTs which require the high-fidelity modeling of the physical system [4] in order to guarantee that the digital asset is able to mirror the real-time state of the physical asset.

(3) Data-driven approaches have been attracting attention recently in wind modeling and prediction [43–45]. These approaches range from simple machine learning (ML) methods [46,47] to specifically-designed deep learning (DL) models to achieve better performance in data mining [48]. The latest developments in DL for wind predictions include the use of transformer neural networks integrated with spatiotemporal correlations [49], the combination of transformer model with wavelet transform [50], Bayesian deep learning approach for uncertainty quantification [51], and multi-modal learning with abnormal data detection capability via stacking DL model [52]. However, these state-of-the-art DL approaches are designed to learn only from data. As the goal of developing a wind farm DT is to predict the full field over the entire farm site with only sparse scattered sensor measurements available, it is thus infeasible to achieve this using these supervised learning approaches.

Here we propose a novel data and knowledge fusion approach to create the first DT for wind farm flow system, where measurement data is used to provide essential information about the real-time flow state and the dynamics not in the data is rediscovered by the flow physics. Specifically, the DT integrates the sparse line-of-sight (LoS) measurements from commercially available Lidar devices [53], Navier–Stokes (NS) equations for the underlying physics of the wind farm wake flows, and actuator disk representations of rotors [54,55], based on physics-informed deep learning [56,57], a sub-field of machine learning just emerging but already seeing exciting successes [58–60]. Its use in wind energy research was introduced in [61,62] where the incoming wind in front of a single wind turbine was studied, while this work focuses on the entire wind farm with wake interactions. The DT in this work can take advantage of deep learning model's capability in handling systems with extreme complexity, strong nonlinearity, and high dimensionality, while making the most use of measurements and physics that are realistically available from the current wind technologies. By fusing data and physics into deep learning, the DT is trained to retrieve the wind speed vector field in the entire wind farm site, based on only sparse measurements.

A set of simulation cases are carried out to demonstrate the developed DT, where SOWFA [63] is used as the platform for numerical experiments [64,65]. From the simulations, the sparse Lidar data and the spatiotemporal wind field in the entire domain are recorded, where the latter only serves as the ground truth (not as training data) to validate the DT's accuracy. The prediction results show that the developed DT is accurate for all the studied conditions, i.e. a greedy case, a wake-steering case, and a partially-operating case. Specifically, the full fields covering the wind farm site are predicted very accurately, showing that the digital mirroring of real-world wind farm from the physical space to the virtual space is established. Then the rotor-effective speed along the turbines' centerlines and the instantaneous speed profiles are extracted from the DT. Very good agreement with the true values is observed. Further analysis shows that the DT is able to capture the in situ unsteady flow features accurately, including wake deficit, wake deflection, wake recovery, and more importantly, wake meandering. Our contributions are listed below.

(1) **A first digital twin for wind farm flow system is developed in this work, which can serve as the backbone of the next-generation wind technology throughout the lifecycle of wind farms.** It achieves the prediction of the in situ spatiotemporal wind farm flow field for the first time, therefore paving ways for brand new research in the areas of DT-enabled wind farm monitoring, wind farm control, load assessment, maintenance scheduling, and power forecasting. The comparison of the developed digital twin with existing numerical, analytical, and data-centric approaches is summarized in Table 1.

(2) **A data and knowledge fusion approach is proposed to establish the wind farm DT, which integrates, in a unified manner, the Lidar measurements, the wind aerodynamics described by Navier–Stokes equations, and the turbine modeling using actuator disk method, via physics-informed deep learning technique.** This data-knowledge-fusion approach also provides important inspirations for developing digital twins for other physical systems (such as wave and tidal energy systems).

(3) **The wind farm DT is validated through a set of high-fidelity numerical experiments, including a greedy case, a wake-steering case, and a partially-operating case.** For all the considered conditions, the full fields covering the wind farm site are all predicted accurately.

In the following parts, Section 2 introduces the DT methodology, Section 3 gives the numerical results, and Section 4 concludes the paper.

2. Methodology

The data and knowledge fusion approach for establishing the wind farm DT is presented in this section, where the overall framework is described first, then a Lidar module (which handles the sensor measurements), an NS module (which considers the wind aerodynamics through NS equations), and a turbine module (which handles the turbine measurements through turbine modeling) are described in detail. The overall method is demonstrated in Fig. 1.

2.1. Data and knowledge fusion framework

The wind farm DT is developed by integrating the Lidar measurements and the physical knowledge seamlessly via the physics-informed learning technique. First, a neural network (NN) is devised to approximate the wind farm flow state. The deep NN, denoted as $\mathcal{N}$, is expressed as

$$[u, v, p] = \mathcal{N}([x, y, t]; W) \tag{1}$$

where $[x, y]$ represents the spatial coordinate in x and y directions in the Cartesian system, t represents the temporal coordinate, W is the trainable weights, and $[u, v, p]$ represents the speed along x and y axes and static pressure. Given any spatial coordinate $[x^*, y^*]$ in the wind farm site and the temporal coordinate t^* as the NN input, the NN returns wind speed and static pressure $[u^*, v^*, p^*]$ at this location and this time instant as the NN output.

Table 1
The comparisons of the developed digital twin with numerical simulations, analytical models, and data-centric approaches.

Type	Analytical models	Numerical simulations	Data-driven methods	The digital twin in this work
Based on	Physical observations	NS equations + turbine modeling	Measurements	Measurements + NS equations + turbine modeling
Approach	Flow analysis	CFD	Machine learning	Physics-informed machine learning
Flow details	No	Yes	No	Yes
Digital mirroring of flow fields	No	No	No	Yes
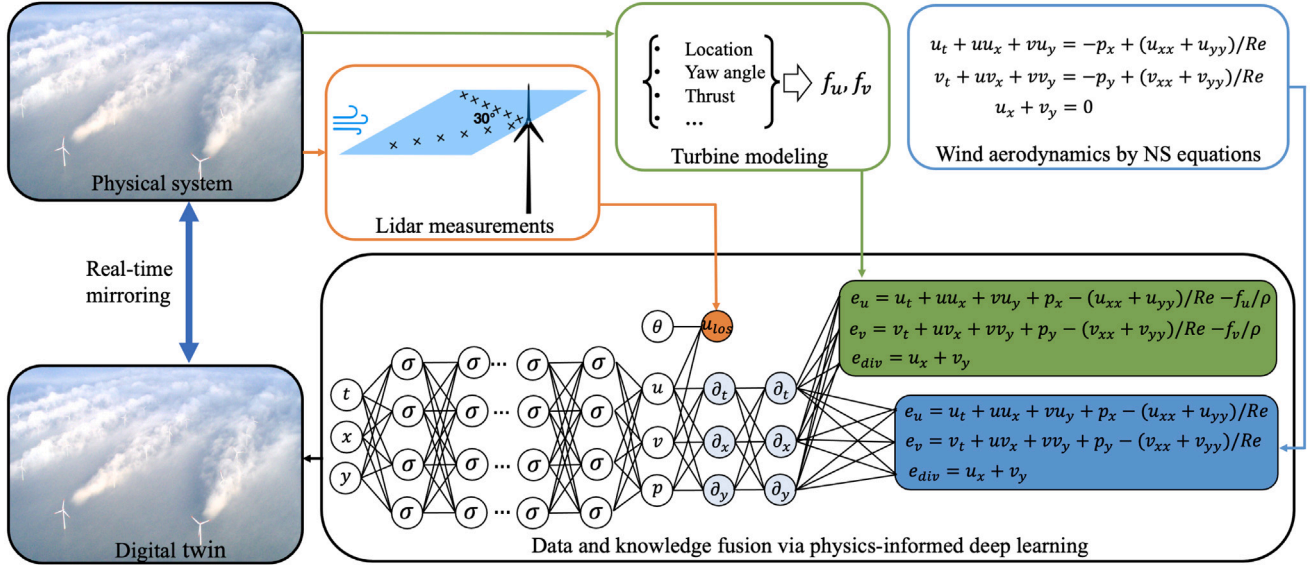
Fig. 1. The proposed data and knowledge fusion framework for establishing the wind farm digital twin (wind farm photo by Christian Steiness).

However, the current sensor technology in wind industry cannot measure the full field in the entire wind energy site. Supervised machine learning is therefore infeasible for the training of $\mathcal{N}$. Moreover, due to the complexity (i.e. the multiple scales and the strong non-linearity) of the wind farm flow system, a very deep NN structure and a very large degree of freedom are typically required for $\mathcal{N}$. This makes its training even more challenging. To tackle these challenges, the approach proposed in this paper combines various realistically-available wind and turbine measurements with physical knowledge of the flow dynamics. By incorporating flow physics, the training of the resulting machine learning model does not need the full field data while it can predict the full field after training. Specifically, different modules are developed to handle different sources of data and physics, and then the training of $\mathcal{N}$ aims at minimizing the loss function L which is defined as

$$L = L_{Lidar} + L_{NS} + L_{Turb}. \tag{2}$$

Here L_{Lidar}, which is the loss derived from the Lidar module, is used to guide the deep NN model to match the Lidar measurements. L_{NS}, which is the loss derived from the NS module, is used to guide the deep NN model to satisfy the physical constraints (such as the conservation of mass and momentum) imposed by the NS equations. And L_{Turb}, which is the loss derived from the turbine module, is used to guide the deep NN to learn from rotors' impact based on turbine parameters (such as turbine locations, yaw angles, and real-time measurements of rotor thrust). The details of each module are given below.

2.2. Lidar module

Turbine-mounted Lidar device provides limited yet valuable real-time wind information in front of the wind turbines. Here it plays the role of informing the DT regarding real-time flow states of the wind farm.

The Lidar configurations in this work are designed based on the specifications of the turbine-mounted Lidar devices developed by ZXLidars [53]. The Lidar range is set as 550 m. The interval is 30 m and there are 17 measurement ranges. It is further configured to scan in the hub-height plane with an opening angle of 42 degree and a resolution of 3.5 degree in the azimuthal direction, resulting in a total number of 13 locations for a whole scanning cycle. This is specified based on the TM-300 [53]. Also, due to the limitation of the commercially available devices, the Lidar considered in this work is set to measure one azimuthal location every 0.5 s which results in a period of 6.5 s for a scanning cycle. The Lidar measurement is therefore very low resolution compared to the dynamic wind farm flow system.

Each data sample of the LoS wind speed measurement is hereby denoted as

$$d^\mu = [x^\mu, y^\mu, t^\mu, \theta^\mu, u^\mu] \tag{3}$$

where u^μ represents the LoS measurement signal at the location $[x^\mu, y^\mu]$ and the time instant t^μ with the Lidar beam's azimuthal angle as θ^μ. The designed Lidar system can provide a dataset for 34 locations per second.

A Lidar module is then developed to make use of the Lidar dataset in the DT. To achieve this, an observation layer is added on top of the deep NN $\mathcal{N}$, as illustrated in Fig. 1. This layer's input is the concatenation of the output of the deep NN $\mathcal{N}$ and beam's azimuthal angle. The output is the LoS wind speed. It is calculated as

$$u^{LoS} = \mathcal{N}([x, y, t])[1]\cos(\theta) - \mathcal{N}([x, y, t])[2]\sin(\theta) \tag{4}$$

where θ is the azimuthal angle of the Lidar beam. L_{Lidar} is then defined by

$$L_{Lidar} = \text{MSE}(U^{LoS} - U^\mu) \tag{5}$$

where MSE represents mean squared error, $U^{LoS} = \{u^{LoS}([x_i^\mu, y_i^\mu, t_i^\mu, \theta_i^\mu]), 0 < i < 1 + N_\mu\}$ is the Lidar module output, and $U^\mu = \{u_i^\mu, 0 < i < 1 + N_\mu\}$ is Lidar measurements.

2.3. NS module

The Lidar module only involves the Lidar measurement locations, which are very sparse both in time and in space. For most part of the domain in the wind farm, no measurements are available. To rediscover the wind information at these locations not measured by Lidar, it is necessary to take the flow physics into account. In this paper, this is achieved by deriving an NS module based on the deep NN $\mathcal{N}$ to enforce the deep NN-predicted flow field to satisfy the underlying physics described by the NS equations.

First, the NS equations are reformulated to obtain e_u, e_v, and e_{div} (as defined in the blue part of Fig. 1). Then the NS module is derived to calculate the functional loss term e_u, e_v and e_{div}. Specifically, e_u, e_v and e_{div} are derived using gradients of the mapping $\mathcal{N}$. This is achieved by using automatic differentiation for computational graphs, which is widely available in all major machine learning libraries (such as the tf.gradients functionality in Tensorflow). All the gradient terms in e_u, e_v and e_{div} are obtained in this way based on the deep NN $\mathcal{N}$. The resulting functional loss terms thus have the same input and the same training variables as $\mathcal{N}$. The loss function L_{NS} can be finally obtained as

$$L_{NS} = \text{MSE}(E_u) + \text{MSE}(E_v) + \text{MSE}(E_{div}) \tag{6}$$

where

$$
\begin{aligned}
E_u &= \{e_u([x_i^{ns}, y_i^{ns}, t_i^{ns}]), 0 < i < 1 + N_{ns}\};\\
E_v &= \{e_v([x_i^{ns}, y_i^{ns}, t_i^{ns}]), 0 < i < 1 + N_{ns}\};\\
E_{div} &= \{e_{div}([x_i^{ns}, y_i^{ns}, t_i^{ns}]), 0 < i < 1 + N_{ns}\}
\end{aligned}
\tag{7}
$$

$\{[x_i^{ns}, y_i^{ns}, t_i^{ns}], 0 < i < 1 + N_{ns}\}$ is randomly sampled from the entire wind farm site (excluding the domain nearby the turbine rotors). It is at these locations and time instants that the physical constraints imposed by NS equations are enforced.

2.4. Turbine module

The flow behind turbine rotors depends greatly on the turbine operating conditions such as yaw angles, the thrust, etc. The key quantities characterizing the turbine rotors' impact on the flow field have been investigated extensively in the context of wake modeling [66,67] and control [68,69]. However, the consideration of real-time turbine information in reconstructing the dynamic wind field has not been investigated yet. This section thus focuses on the development of a turbine module, which first transforms the turbine operating conditions as physical constraints via turbine modeling, and then integrates the constraints into the developed wind farm DT through the loss function L_{Turb}.

The turbine modeling in this work follows the actuator disk approach [54,55]. Here the force exerted by the actuator disks is filtered by a Gaussian kernel before being applied to the fluid volume. Specifically, the force on the fluid volume is calculated based on the real-time turbine thrust as

$$f(x, y) = -\sum_{i=1}^{N_{ad}} \frac{f_i}{\epsilon^2 \pi} \exp\left(-\frac{|x - x_i^f|^2 + |y - y_i^f|^2}{\epsilon^2}\right) \tag{8}$$

where $[x, y]$ represents the location of the fluid volume, N_{ad} represents the total number of the elements in the actuator disk, $[x_i^f, y_i^f]$ and f_i represent the location and the actuator force of the ith discretized actuator element, and ϵ represents the smoothing parameters of the Gaussian kernel. Then the force is projected in x and y directions as

$$f_u = f \cos(\gamma) \tag{9}$$

and

$$f_v = f \sin(\gamma) \tag{10}$$

where γ is the yaw angle of each turbine. The functional loss terms arising from the momentum equations with the volume forces can thus be obtained as

$$\tilde{e}_u = e_u - \frac{f_u}{\rho}$$

$$\tilde{e}_v = e_v - \frac{f_v}{\rho}.$$

where ρ is the air density. Finally, the loss function that incorporates the turbine rotors' impact on the flow field is obtained as

$$L_{Turb} = \text{MSE}(\tilde{E}_u) + \text{MSE}(\tilde{E}_v) + \text{MSE}(E_{div}) \tag{11}$$

where

$$
\begin{aligned}
\tilde{E}_u &= \{\tilde{e}_u([x_i^T, y_i^T, t_i^T]), 0 < i < 1 + N_{Turb}\};\\
\tilde{E}_v &= \{\tilde{e}_v([x_i^T, y_i^T, t_i^T]), 0 < i < 1 + N_{Turb}\};\\
E_{div} &= \{e_{div}([x_i^T, y_i^T, t_i^T]), 0 < i < 1 + N_{Turb}\}
\end{aligned}
\tag{12}
$$

$\{[x_i^T, y_i^T, t_i^T], 0 < i < 1 + N_{Turb}\}$ is a batch of test points randomly sampled from the domain near the turbine rotors. It is at these locations and time instants that the modeling of turbines' impact on the flow field is taken into account.

2.5. Model construction, training and prediction

By minimizing the loss function L, the DT learns from the Lidar measurements, the wind aerodynamics described by NS equations, and the turbine rotors' impact on the wind flow simultaneously. In this work, a large and deep fully-connected NN is constructed for $\mathcal{N}$ so that it can capture detailed flow dynamics. The final NN structure is set as 3-128-128-128-128-128-128-128-128-128-3. The Adam optimizer [70] is used with a learning rate of 10^{-3}. After training, the spatial coordinates corresponding to a uniform mesh covering the entire wind farm (e.g. a 12 m × 12 m mesh) are fed directly to the DT to predict the full spatiotemporal fields, therefore establishing the digital mirroring to the physical flow system.

3. Results and discussions

The evaluation of the DT is carried out through high-fidelity numerical experiments. In the following parts, the simulation setups are described first. Then a set of typical wind farm operation scenarios are investigated, including a greedy case, a wake-steering case, and a partially-operating case.

3.1. Simulation details

The simulations use a high-fidelity solver called SOWFA, which is developed by NREL for the scale-resolving simulation of wind farm wake flows [64,65]. In this section, an example site with six turbines is investigated, which is illustrated in Fig. 2. The turbine type is the NREL 5MW and it has a diameter (denoted as D hereafter) of 126.4 m. The spanwise spacing is $3D$ and the streamwise spacing is $5D$. A precursor turbulent atmospheric flow simulation is carried out to prepare a 10 m/s, southwest wind flow. Then the simulations of wind farms are carried out under such precursor flow. The computational domain, as illustrated by Fig. 2 (which shows the top view of the horizontal plane at the turbine hub height) and Fig. 3 (which shows the 3D flow domain), extends 3 km in south–north direction, 3 km in west–east direction, and 1 km in vertical direction. Such a domain size is set up in order to ensure proper development of the atmospheric boundary layer flows [71]. For mesh generations, uniform mesh is used with two-level mesh refinement. As shown in Fig. 2, in the outer
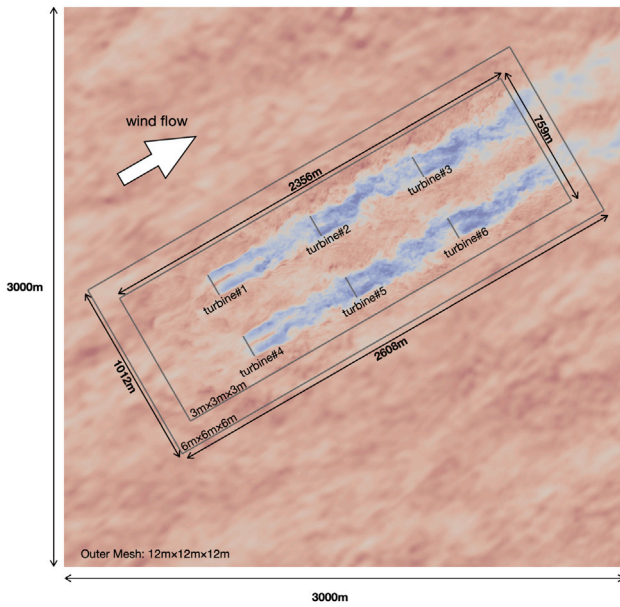
Fig. 2. The computational domain and the corresponding mesh.

Fig. 3. The three-dimensional flow field by the vorticity isosurface.

region which covers most of the flow domain, the grid size is set as 12 m × 12 m × 12 m. In the wind turbine wake region, the grid size is set as 3 m × 3 m × 3 m. And the grid size is set as 6 m × 6 m × 6 m for the region in-between. The local refinements in the vertical direction take place at 279 m and 405 m respectively, as suggested by the work [13]. The grid size of 3 m is set according to the recommendations by the developers in order to resolve the detailed flow dynamics in the wake region [13]. The boundary condition is set by the surface stress and temperature flux model as well as zero normal velocity for the bottom boundary, and the zero stress and temperature flux as well as zero normal velocity is set for the top boundary, which are typical for simulating atmospheric flows [64]. As for the lateral boundaries, inflow and outflow conditions are imposed for the west and east boundaries respectively, while the cyclic condition is imposed for the north and south boundaries. As for the time discretization, the time step is set as 0.02 s so that the rotor blades' motion can be well captured with blade elements moving less than one grid cell per time step. The simulation is carried out for a period of 700 s for each case. About 7680 CPU hours are needed for one simulation case based on the Avon clusters at the University of Warwick. Fig. 2 illustrates an instantaneous velocity field while Fig. 3 shows a three-dimensional flow field by the vorticity isosurface. As shown, the large-scale as well as the small-scale flow structures are all captured very well in the simulated flow fields, demonstrating the scale-resolving capability of the numerical experiment platform. From the wind farm simulations, the first 300 s simulations are discarded, as the wake flow generated by the wind turbines has not been well established. From the last 400 s simulations, Lidar measurements are extracted. The Lidar measurement data, along with the turbine locations, turbine yaw angles and rotor thrust measurements, is used for the training of the wind farm DT. The entire flowfields are also recorded. They are assumed unknown during the training process and only used as the test dataset to evaluate the accuracy of the developed DT.

3.2. Greedy case

The greedy case, which is the most common scenario in the current wind industry, is considered first. In this case, the turbine yaw direction is set as the same as the incoming wind direction, so that each individual wind turbine extracts most of energy for its own (thus called greedy).
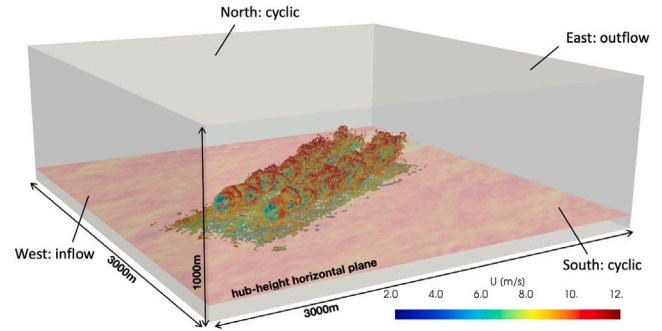
The DT-predicted full fields over the wind farm site (which correspond to the virtual entity) are compared with the full fields given by SOWFA (which correspond to the physical entity). Fig. 4(a) and 5(a) show two example snapshots, and the corresponding unsteady flow visualization is given in Video 1. Clearly, the DT predicts the dynamic full fields very accurately, including both the freestream flow and the flow behind wind turbines. In particular, spatiotemporal variability of the incoming wind field, wake flows behind wind turbines, and their downstream propagation, are all captured very well. Furthermore, the meandering of the flow structures in y direction is also captured well, which can be seen most clearly by the second-column turbines' far wake. It is worth mentioning that wake meandering has been widely studied in the literature due to its large influence on the wind turbine energy production and structural load [72,73]. However, to date, to the authors' knowledge, there are no studies that achieved the in situ full field reconstruction capturing the unsteady wake meandering based on measurements. For the first time, the results here demonstrate that it is possible to achieve this using commercially available Lidar device.

On the other hand, the full field comparisons illustrate the DT is not capable of capturing the very small-scale flow structures, which are smoothed out in the predicted flow fields. This is reasonable, as the only wind measurements used in the developed DT is the Lidar measurements, which has a very low resolution both in space (the distance between neighboring measurement points is 30 m) and in time (the time interval for measuring the same azimuthal location is 6.5 s). We mention, however, that the inability in capturing very small-scale flow structure does not undermine the developed DT's usefulness in most of the practical scenarios where large-scale flow structures in the wind are of main interest.

From the DT-predicted wind field, various wind information can be extracted. Here, to further demonstrate the performance of the developed DT, the rotor-effective speed along turbine centerlines, which determines power generation, is examined. It is computed by

$$U_{eff}(x,t) = \frac{1}{N_Y}\sum_{i=1}^{N_Y} U(x, Y+y_i, t) \qquad (13)$$

where Y is the lateral coordinate of the turbine location, and $\{y_i, 0 < i < 1+N_y\}$ covers the interval $[-D/2, D/2]$. Fig. 4(b-c) and 5(b-c) show the DT predictions and the ground truth. Figs. 4(b) and 5(b) give the rotor-effective speed for the first-row wind turbines, and Figs. 4(c) and 5(c) are for the second-row turbines. As shown, the DT predictions are very close to their true values. Turbine location is also marked, as shown by the dotted blue lines in Fig. 4(b, c) and Fig. 5(b, c). Clearly, the turbine rotors' impact on the flow is captured by the developed wind farm DT, where the wake deficit, i.e. the drastic speed decrease due to turbines' presence, and the wake recovery, i.e. the gradual speed recovery while the wake develops and mixes with freestream wind flows, are both predicted accurately. Moreover, as shown by both field visualizations and effective speeds, the flows at different time instants have clear quantitative differences. This unsteadiness is captured accurately, as
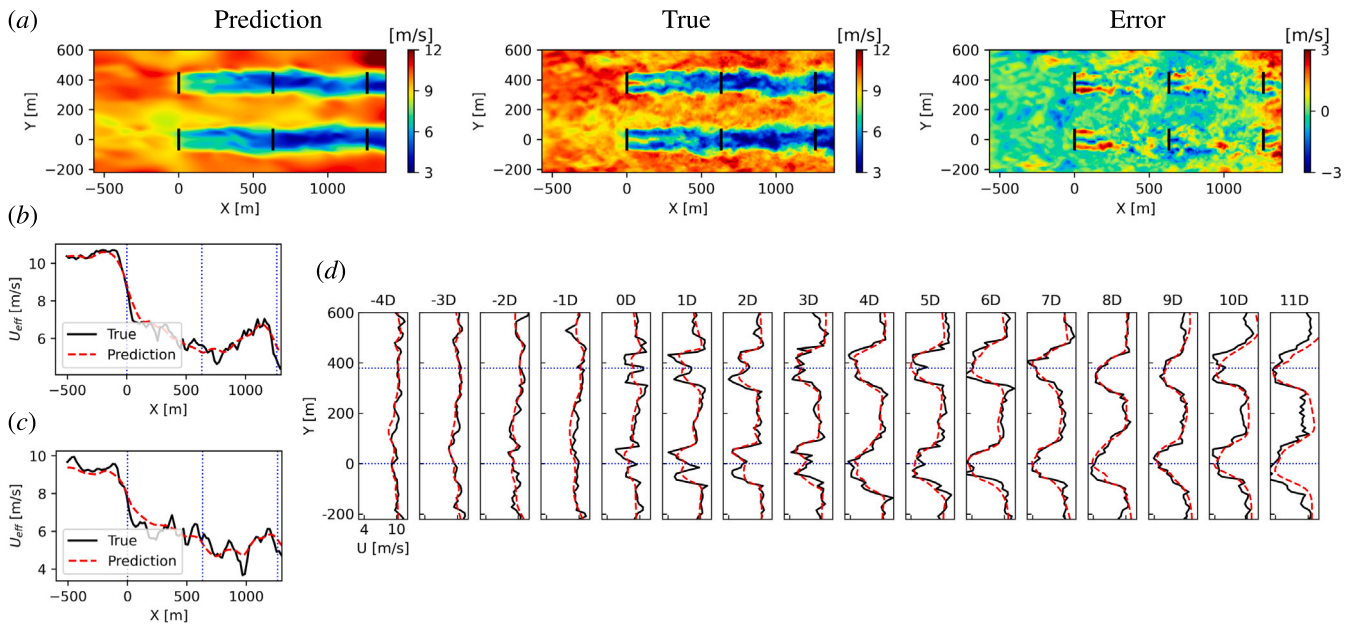
Fig. 4. The DT predictions for the greedy case at $t = 200$ s. (a) the full field; (b) the rotor-effective speed for the upper-row turbines; (c) the rotor-effective speed for the lower-row turbines; (d) the speed profiles.
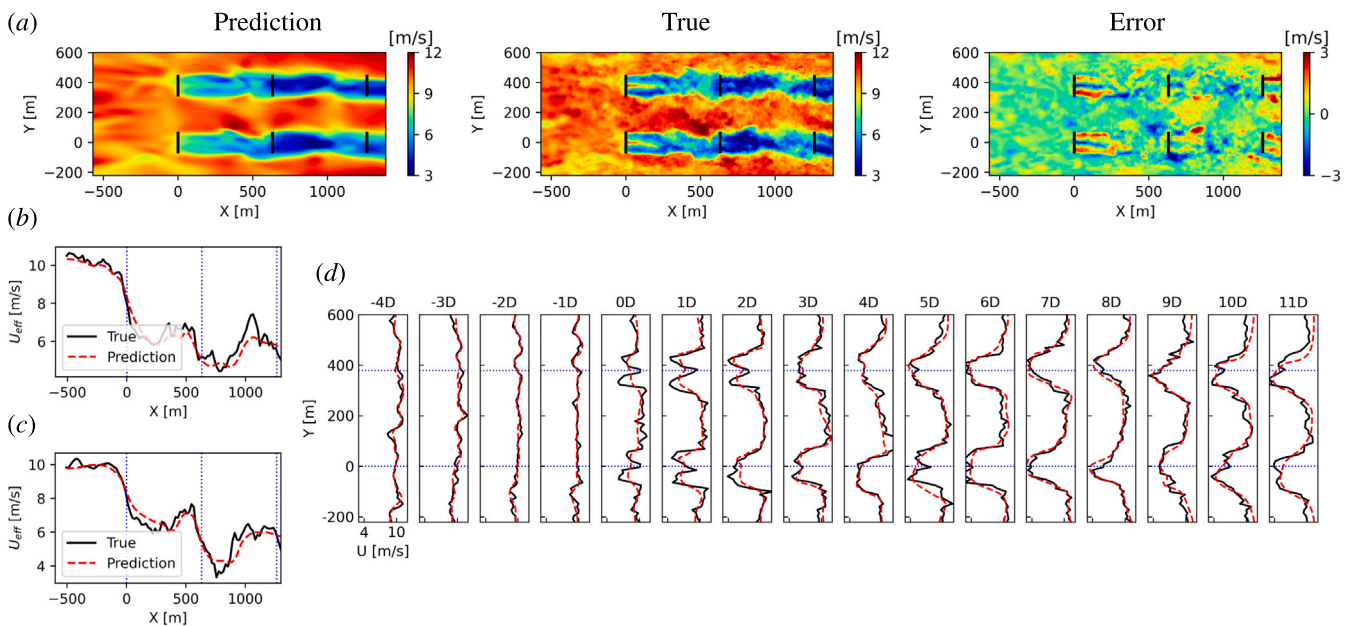

Fig. 5. The DT predictions for the greedy case at $t = 400$ s. (a) the full field; (b) the rotor-effective speed for the upper-row turbines; (c) the rotor-effective speed for the lower-row turbines; (d) the speed profiles.

demonstrated by the good match between the DT predictions and the ground truth at different time instants throughout the time period.

Next, the speed profiles are extracted based on full fields predicted by the DT. The results are given in Fig. 4(d) and 5(d). As shown, the speed profiles are predicted very accurately, including the flow details of the freestream turbulent wind (as shown by the profiles from X = -4D to X = -1D), the wakes generated by individual turbines (as shown by the profiles from X = 0D to X = 4D), and the wake-wake interactions (as shown by the profiles from X = 5D onward). Particularly, the wake deficit due to the turbine inductions, at X = 0D, X = 5D, and X = 10D, and the wake recovery that follows, are all captured very well, such as the development of the wake profiles from 'double-peak' towards 'single-peak' shapes and the wake profiles' expansions along y direction. More specifically, wakes behind the second-column turbines

develop faster than the front turbine wakes, because of the enhanced mixing due to wake-wake interactions. For example, the 'single-peak' profile is formed at approximately 4D downstream of the front turbine wakes, while formed at approximately X = 7D which is 2D downstream of the second-column turbines. In addition, the performance of the developed DT in capturing the effects of wake meandering is also clearly demonstrated through these speed profiles. For example, as shown by the profile at X = 8D in Fig. 4(d), the wake center at the upper row meanders downward in the spanwise direction at this time instant (i.e. t = 200s), while at t = 400 s, as shown in Fig. 5(d), the wake center at the same location meanders upward. To summarize, a great match between the predicted profiles and the ground truth is observed, demonstrating clearly the performance of the developed DT in capturing detailed flow features.
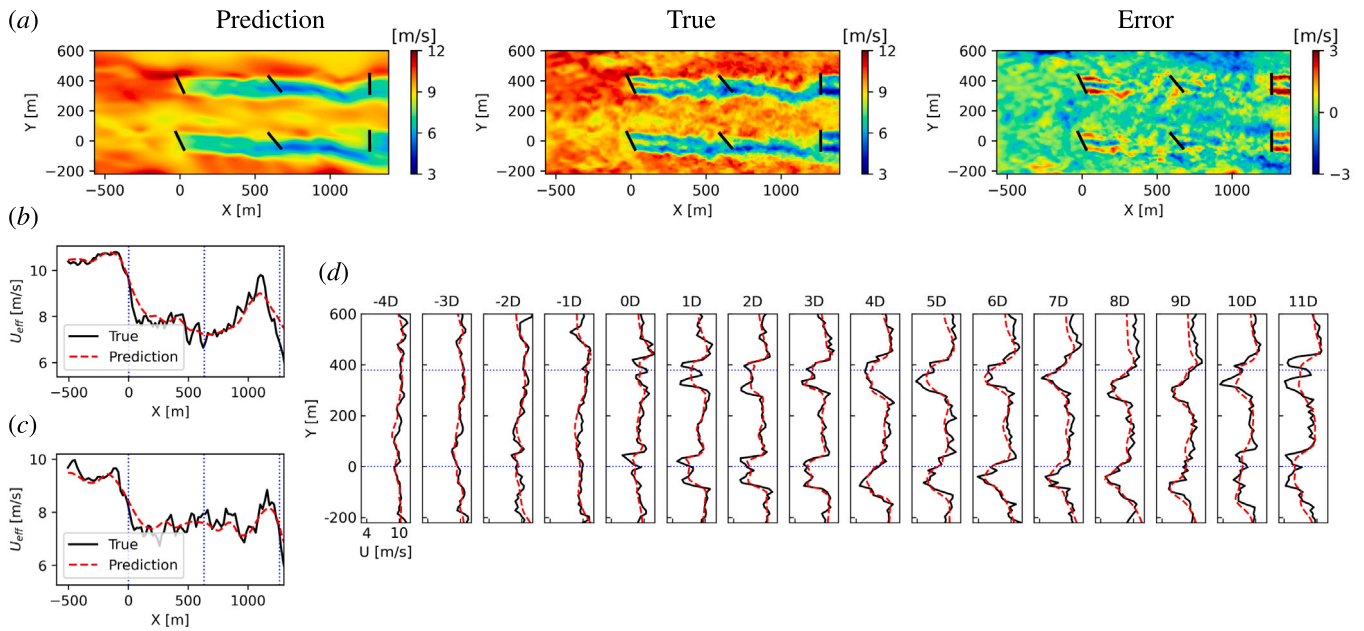
Fig. 6. The DT predictions for the wake-steering case at $t = 200$ s. (a) the full field; (b) the rotor-effective speed for the upper-row turbines; (c) the rotor-effective speed for the lower-row turbines; (d) the speed profiles.

Table 2
RMSEs of the DT-predicted full fields for all three cases. Case #1, #2 and #3 represent the greedy case, the wake-steering case, and the partially-operating case. u and v are wind components in x and y directions.

Case	Quantity	Value range	RMSE (% of range)
#1	u (m/s)	[0.437, 14.1]	0.677 (5.0%)
	v (m/s)	[−5.42, 5.05]	0.434 (4.1%)
#2	u (m/s)	[1.12, 13.8]	0.656 (5.2%)
	v (m/s)	[−5.61, 4.31]	0.490 (4.9%)
#3	u (m/s)	[0.539, 13.6]	0.586 (4.5%)
	v (m/s)	[−5.31, 5.11]	0.392 (3.8%)

We mention, however, that for the profiles in the near wake region, there exists a moderate discrepancy between the prediction and the ground truth. This can be also seen from the error distributions in the near wake region as shown in Fig. 4(a) and 5(a). This is not unexpected, because the developed DT incorporates the sparse Lidar measurements, which are not available in this region, and the actuator disk turbine model, which has no detailed representations of the turbine blades. Thus the local impact of the turbine blades in this region is neither measured nor modeled. In practice, more powerful Lidar devices, along with advanced structural sensors and more complex turbine modeling approaches, may be used to accurately predict the flow details in this region. However, this will bring much more cost to the developed DT system and greatly reduce its flexibility due to the requirement of detailed blade information. The present DT system only requires Lidar measurements, turbine location, turbine yaw angle, and rotor thrust. Thus it can be easily applied to a general wind farm consisting of generic wind turbine types. It is also worth mentioning that the far wake region, where good accuracy is achieved by the developed DT, is the main region of interest in many applications such as wind farm monitoring, control, and power forecasting.

Root mean square errors (RMSE) of DT-predicted full fields are calculated next. They are reported in Table 2 for both u and v components. The value ranges of the corresponding wind velocity components are also given in Table 2. As shown, the RMSE is just 5.0% of the value range for the streamwise velocity field while it is just 4.1% for the spanwise velocity field, demonstrating the great accuracy of the developed DT.

3.3. Wake-steering case

Wake steering has been investigated recently for the coordinated control of wind turbines to mitigate the wake effects thus achieving optimal performance for the overall wind farm [14,16]. This second case study thus considers the DT's performance in an optimized yaw control scenario. In particular, according to the optimization results reported by Gebraad et al. [14], the turbine yaw angles in this case are set as 25.15, 39.75, 0.45, 25.85, 39.80, and 0.35 degrees from the turbine #1 to the turbine #6 respectively (the turbine numbers are illustrated in Fig. 2).

First, the DT-predicted dynamic full fields are shown in Fig. 6(a) and 7(a) and in Video 2. As shown, as in the case of greedy wind farm, the full fields are predicted very accurately for this wake-steering case. Flow structures such as wake deficit, deflection, and meandering, are all captured very well by the developed DT.

The rotor-effective speed is then calculated based on full fields obtained by the DT, which is shown in Fig. 6(b, c) and 7(b, c). As shown, the results predicted by the DT are very accurate. In particular, the speed decrease along the centerline is less dramatic in this case than the greedy case, demonstrating that the wake-steering yaw control is working as expected (which means, by wake steering, the downstream turbines now operate in a much more favorable wind condition with a much higher rotor-effective speed than their greedy counterparts). The wake-steering effects can also be clearly seen from the speed profiles, which are shown in Fig. 6(d) and 7(d). The development of the profiles clearly shows that turbine wakes propagate in the deflected directions due to the yaw effects, which is successfully captured by the developed DT. To summarize, the developed DT captures the detailed flow features accurately in this wake-steering case, similar as in the greedy case.

We mention that recently wind farm yaw control has been investigated in numerous field test studies and various levels of power capture improvement were reported, such as the power increase up to 29% for a downstream turbine [74], a 4% increase in energy production of the two-turbine case [75], the performance gains of 35% for two-turbine interactions and up to 16% for three-turbine interactions [76]. However, an in-depth analysis of the quantitative link between the wake steering and the power generation is hindered by the lack of the in situ dynamic full field information in real-world wind farms. The case
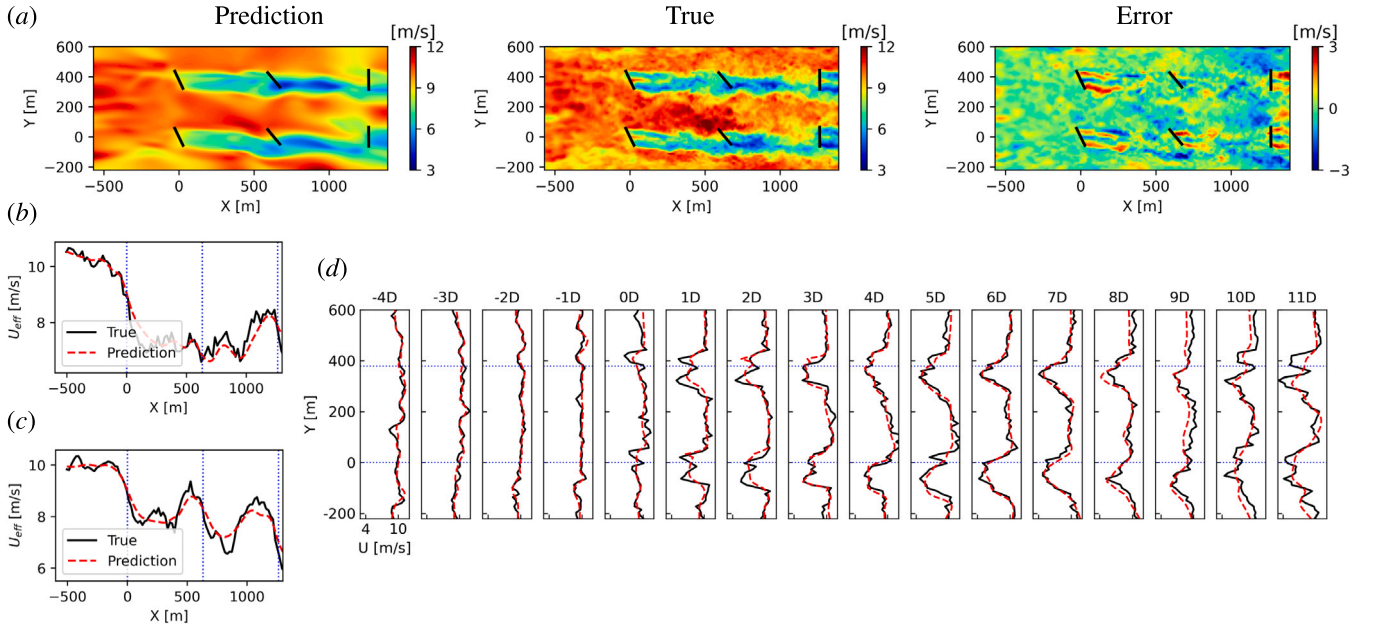
Fig. 7. The DT predictions for the wake-steering case at $t = 400$ s. (a) the full field; (b) the rotor-effective speed for the upper-row turbines; (c) the rotor-effective speed for the lower-row turbines; (d) the speed profiles.
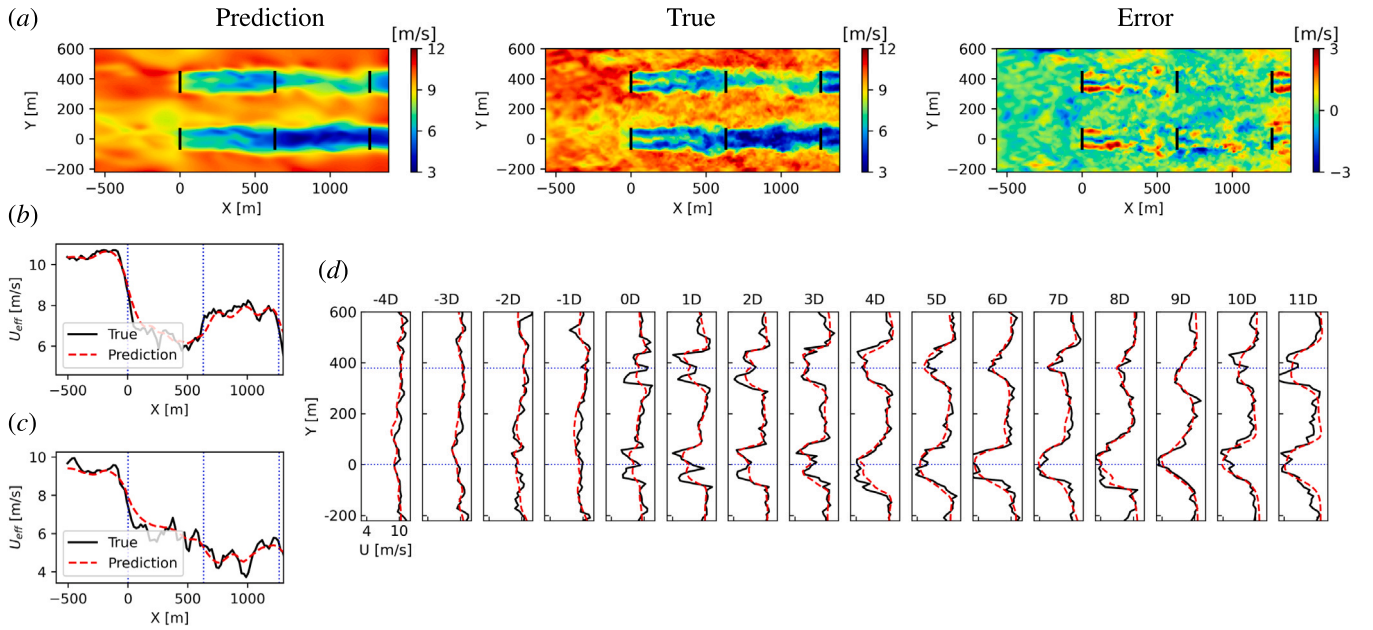

Fig. 8. The DT predictions for the partially-operating case at $t = 200$ s. (a) the full field; (b) the rotor-effective speed for the upper-row turbines; (c) the rotor-effective speed for the lower-row turbines; (d) the speed profiles.

study here demonstrates that, based on the developed DT, it is possible to tackle this issue using only commercially-available measurement devices.

RMSEs of the DT predictions are also given in Table 2 for this wake-steering case. As shown, similar as in the greedy case, the prediction errors are very small, demonstrating great accuracy achieved by the developed DT.

3.4. Partially-operating case

Real-world wind farms are subject to various disruptions such as wind turbine fault, scheduled maintenance, etc. In such scenario, parked turbines often co-exist with other operational turbines. The

third case focuses on such partially-operating scenario. Particularly, the same wind farm consisting of six greedy turbines is considered, where the turbine #2 (i.e. the second turbine in the first row) is now in parked condition.

First, the dynamic full fields are given in Fig. 8(a) and 9(a) and in Video 3. As in the other two cases, the fields covering the entire wind farm, including both the inflow and the turbine wake, are predicted very accurately. Because the turbine #2 is now in parked condition which does not extract power from the wind, the flow in the first row has a clearly larger wind speed magnitude than the second row.

Next, Fig. 8(b, c, d) and 9(b, c, d) show the rotor-effective speed along the centerline and the speed profiles. A good match between the prediction and the ground truth is observed. The rotor-effective
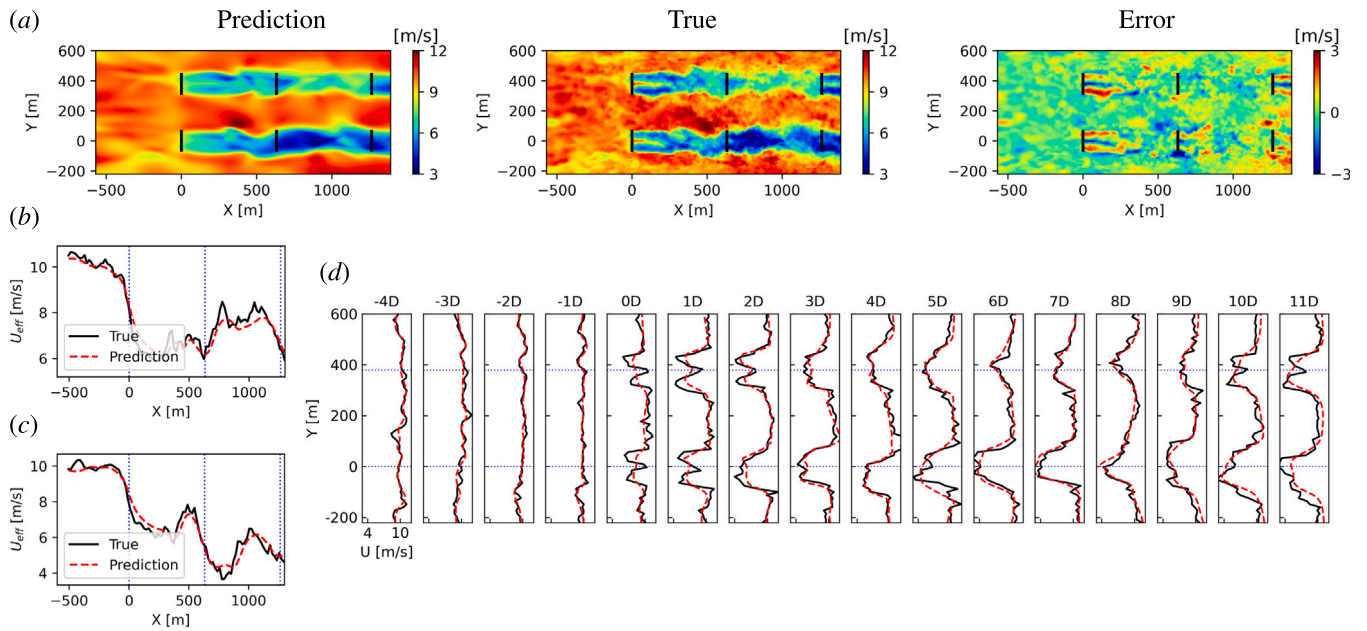
Fig. 9. The DT predictions for the partially-operating case at *t* = 400 s. (a) the full field; (b) the rotor-effective speed for the upper-row turbines; (c) the rotor-effective speed for the lower-row turbines; (d) the speed profiles.

speed in the first row of turbines, as shown in Fig. 8(b) and 9(b), recovers towards freestream wind speed and reaches about 8 m/s before decreasing again due to the turbine in the third column, while the rotor-effective speed in the second row, as shown in Fig. 8(c) and 9(c), is much lower than the first row, due to the momentum extraction by the turbine at X = 5D. The details of the wake development, such as the faster recovery of the wake in the first row compared to the second row, are also captured very well by the developed DT which can be seen from the speed profiles in Fig. 8(d) and 9(d).

Finally, RMSEs for this case are also reported in Table 2. As in other cases, great accuracy is obtained for this partially-operating case, demonstrating the developed DT's versatility in various scenarios of practical interest.

3.5. Discussions

The results in this section clearly demonstrate that the proposed wind farm DT is able to predict the spatiotemporal flow fields covering the wind farm site at various operating scenarios accurately. From the traditional machine learning point of view, this is an unsupervised ML problem. The accurate flow prediction achieved by the DT, including the successful characterization of wake interactions and wake meandering, is very challenging, as this is an ill-posed inverse problem involving a complex multi-scale nonlinear flow system. The design that enables the current DT performance lies in the information fusion of the proposed approach, which includes the Lidar measurements, the turbines' operational data (i.e. the location, yaw angle, and rotor thrust), the NS equations characterizing wind aerodynamics, and actuator disk modeling of the impact of the turbine rotors on the flow fields. All these data and physical knowledge are fused into a deep, large neural network model with the capability of approximating complex nonlinear systems. This allows the consideration of all the available information with physical consistency when making predictions for new locations where there are no measurements. Specifically, when making predictions for a new location, the DT implicitly considers the correlations between the location to be predicted and the data points measured by the neighboring Lidar based on NS equations, as well as the correlations between the location to be predicted and the data points measured by different Lidars based on NS equations with actuator disk modeling. It is worth mentioning that the explanations of data correlations are

based on physical intuition instead of rigorous proof, as the whole deep learning model is trained with all the information simultaneously. For readers who are interested in developing DTs for wind and other systems via physics-informed ML approaches, the results in this work suggest that the DT should fuse as much data and physical knowledge as possible into the training of the deep learning model, as long as the fused information from different sources is physically consistent.

4. Conclusions

The first digital twin for wind farm flow system was developed, which seamlessly fuses the sparse flow measurements by commercially available Lidar devices, the wind aerodynamics described by Navier–Stokes equations, and the turbine modeling by actuator disk method. By fusing the scattered sparse measurement of Lidar, which can provide limited but essential information of the real-world wind farm flow field, and the Navier–Stokes equations and actuator disk turbine modeling, which can rediscover the wind aerodynamics that is not captured in the measurements, the DT successfully retrieved the full field in the entire wind energy site.

The developed DT was then validated via numerical experiments. Three typical operating scenarios of wind farms, including a greedy case, a wake-steering case, and a partially-operating case, were included in the validation study. The results showed that for all the cases, the developed DT achieved very accurate mirroring of the physical wind farm flow system. Specifically, the prediction results for the spatiotemporal fields covering the entire wind farm, the rotor-effective speed along wind turbine centerlines, and the speed profiles, demonstrated that flow characteristics including the speed variations of incident wind, wake development in the downstream direction (including its deficit, deflection and expansion), and meandering in the crosswind direction, were all captured very well. The root mean square error of full field predictions showed that the DT was very accurate, i.e. the prediction error for all the cases, on average, was 0.640 m/s and 0.439 m/s for the u and v components respectively, which were just 4.7% and 4.1% relative to the value ranges.

The DT developed, which achieves the accurate in situ full field prediction using commercially-available sensor devices, paves the way for future research in the areas of DT-enabled wind technologies across turbine lifecycle, including assessment, wind farm monitoring, wind

farm control, maintenance scheduling, and power forecasting. Future works may involve the development of the interfaces to facilitate the DT's application in these areas and the DT's deployment on cloud computing platforms. Another direction is to further improve the performance of the DT, such as the extension to full three dimension and the integration with wind turbine structural and electrical models.

CRediT authorship contribution statement

Jincheng Zhang: Conceptualization, Data curation, Formal analysis, Investigation, Methodology, Project administration, Software, Validation, Visualization, Writing – original draft. **Xiaowei Zhao:** Conceptualization, Funding acquisition, Formal analysis, Investigation, Methodology, Project administration, Resources, Supervision, Writing – review & editing.

Data availability

Data will be made available on request.

Acknowledgments

Declaration of competing interest

The authors declare that they have no known competing financial interests or personal relationships that could have appeared to influence the work reported in this paper.

Appendix A. Supplementary data

Supplementary material related to this article can be found online at https://doi.org/10.1016/j.enconman.2023.117507.

References

[1] Council GWE. Gwec| Global wind report 2022. 2022.

[2] Grieves M. Digital twin: Manufacturing excellence through virtual factory replication. White paper 2014;1:1–7.

[3] Tao F, Zhang H, Liu A, Nee AY. Digital twin in industry: State-of-the-art. IEEE Trans Ind Inf 2018;15(4):2405–15.

[4] Glaessgen E, Stargel D. The digital twin paradigm for future NASA and US air force vehicles. In: 53rd AIAA/ASME/ASCE/AHS/ASC structures, structural dynamics and materials conference 20th AIAA/ASME/AHS adaptive structures conference 14th AIAA. 2012, p. 1818.

[5] Cimino C, Negri E, Fumagalli L. Review of digital twin applications in manufacturing. Comput Ind 2019;113:103130.

[6] Wanasinghe TR, Wroblewski L, Petersen BK, Gosine RG, James LA, De Silva O, et al. Digital twin for the oil and gas industry: Overview, research trends, opportunities, and challenges. IEEE Access 2020;8:104175–97.

[7] Yan B, Li Q. Coupled on-site measurement/CFD based approach for high-resolution wind resource assessment over complex terrains. Energy Convers Manage 2016;117:351–66.

[8] Li J, Wang X, Yu XB. Use of spatio-temporal calibrated wind shear model to improve accuracy of wind resource assessment. Appl Energy 2018;213:469–85.

[9] Tang X-Y, Zhao S, Fan B, Peinke J, Stoevesandt B. Micro-scale wind resource assessment in complex terrain based on cfd coupled measurement from multiple masts. Appl Energy 2019;238:806–15.

[10] Lundquist J, DuVivier K, Kaffine D, Tomaszewski J. Costs and consequences of wind turbine wake effects arising from uncoordinated wind energy development. Nature Energy 2019;4(1):26–34.

[11] Hand MM, Balas MJ. Blade load mitigation control design for a wind turbine operating in the path of vortices. Wind Energy: Int J Prog Appl Wind Power Convers Technol 2007;10(4):339–55.

[12] Zhang J, Zhao X, Wei X. Reinforcement learning-based structural control of floating wind turbines. IEEE Trans Syst Man Cybern: Syst 2022;52(3):1603–13. http://dx.doi.org/10.1109/TSMC.2020.3032622.

[13] Fleming P, Gebraad PM, Lee S, van Wingerden J-W, Johnson K, Churchfield M, et al. Simulation comparison of wake mitigation control strategies for a two-turbine case. Wind Energy 2015;18(12):2135–43.

[14] Gebraad PM, Teeuwisse F, Van Wingerden J, Fleming PA, Ruben S, Marden J, et al. Wind plant power optimization through yaw control using a parametric model for wake effects—a CFD simulation study. Wind Energy 2016;19(1):95–114.

[15] Howland MF, Lele SK, Dabiri JO. Wind farm power optimization through wake steering. Proc Natl Acad Sci 2019;116(29):14495–500.

[16] Dong H, Zhang J, Zhao X. Intelligent wind farm control via deep reinforcement learning and high-fidelity simulations. Appl Energy 2021;292:116928.

[17] Nilsson J, Bertling L. Maintenance management of wind power systems using condition monitoring systems—life cycle cost analysis for two case studies. IEEE Trans Energy Convers 2007;22(1):223–9.

[18] Artigao E, Martín-Martínez S, Honrubia-Escribano A, Gómez-Lázaro E. Wind turbine reliability: A comprehensive review towards effective condition monitoring development. Appl Energy 2018;228:1569–83.

[19] Khan MA, Javed A, Shakir S, Syed AH. Optimization of a wind farm by coupled actuator disk and mesoscale models to mitigate neighboring wind farm wake interference from repowering perspective. Appl Energy 2021;298:117229.

[20] Mahoney WP, Parks K, Wiener G, Liu Y, Myers WL, Sun J, et al. A wind power forecasting system to optimize grid integration. IEEE Trans Sustain Energy 2012;3(4):670–82.

[21] Duan J, Zuo H, Bai Y, Duan J, Chang M, Chen B. Short-term wind speed forecasting using recurrent neural networks with error correction. Energy 2020;119397.

[22] Liu Y, Qin H, Zhang Z, Pei S, Jiang Z, Feng Z, et al. Probabilistic spatiotemporal wind speed forecasting based on a variational Bayesian deep learning model. Appl Energy 2020;260:114259.

[23] He R, Sun H, Gao X, Yang H. Wind tunnel tests for wind turbines: A state-of-the-art review. Renew Sustain Energy Rev 2022;166:112675.

[24] Sun H, Gao X, Yang H. A review of full-scale wind-field measurements of the wind-turbine wake effect and a measurement of the wake-interaction effect. Renew Sustain Energy Rev 2020;132:110042.

[25] Zhang W, Markfort CD, Porté-Agel F. Wind-turbine wakes in a convective boundary layer: A wind-tunnel study. Boundary-Layer Meteorol 2013;146:161–79.

[26] Barthelmie RJ, Hansen K, Frandsen STs, Rathmann O, Schepers J, Schlez W, et al. Modelling and measuring flow and wind turbine wakes in large wind farms offshore. Wind Energy: Int J Prog Appl Wind Power Convers Technol 2009;12(5):431–44.

[27] Schepers J, Obdam T, Prospathopoulos J. Analysis of wake measurements from the ECN wind turbine test site wieringermeer, EWTW. Wind Energy 2012;15(4):575–91.

[28] Harris M, Hand M, Wright A. Lidar for turbine control. 2006, National Renewable Energy Laboratory, Golden, CO, Report No. NREL/TP-500-39154.

[29] Shu Z, Li Q, He Y, Chan P. Observations of offshore wind characteristics by Doppler-LiDAR for wind energy applications. Appl Energy 2016;169:150–63.

[30] El-Asha S, Zhan L, Iungo GV. Quantification of power losses due to wind turbine wake interactions through SCADA, meteorological and wind LiDAR data. Wind Energy 2017;20(11):1823–39.

[31] Gao X, Wang T, Li B, Sun H, Yang H, Han Z, et al. Investigation of wind turbine performance coupling wake and topography effects based on LiDAR measurements and SCADA data. Appl Energy 2019;255:113816.

[32] Fan Z, Li S, Gao Z, Zhang L, Zheng X, Zhu W, et al. On the importance of wind turbine wake boundary to wind energy and environmental impact. Energy Convers Manage 2023;277:116664.

[33] Mikkelsen T, Mann J, Courtney M, Sjöholm M. Windscanner: 3-D wind and turbulence measurements from three steerable Doppler lidars. IOP Conf Ser: Earth Environ Sci 2008;1(1):012018.

[34] Sanderse B, Van der Pijl S, Koren B. Review of computational fluid dynamics for wind turbine wake aerodynamics. Wind energy 2011;14(7):799–819.

[35] Porté-Agel F, Wu Y-T, Lu H, Conzemius RJ. Large-eddy simulation of atmospheric boundary layer flow through wind turbines and wind farms. J Wind Eng Ind Aerodyn 2011;99(4):154–68.

[36] Wu Y-T, Porté-Agel F. Modeling turbine wakes and power losses within a wind farm using LES: An application to the horns rev offshore wind farm. Renew Energy 2015;75:945–55.

[37] Mullowney P, Li R, Thomas S, Ananthan S, Sharma A, Rood JS, et al. Preparing an incompressible-flow fluid dynamics code for exascale-class wind energy simulations. In: Proceedings of the international conference for high performance computing, networking, storage and analysis. 2021, p. 1–16.

[38] Boersma S, Doekemeijer BM, Gebraad PM, Fleming PA, Annoni J, Scholbrock AK, et al. A tutorial on control-oriented modeling and control of wind farms. In: 2017 American control conference. IEEE; 2017, p. 1–18.

[39] Jensen NO. A note on wind generator interaction. Citeseer; 1983.

[40] Katic I, Højstrup J, Jensen NO. A simple model for cluster efficiency. In: European Wind energy association conference and exhibition. A. Raguzzi; 1987.

[41] Göçmen T, Van der Laan P, Réthoré P-E, Diaz AP, Larsen GC, Ott S. Wind turbine wake models developed at the technical university of Denmark: A review. Renew Sustain Energy Rev 2016;60:752–69.

[42] Kaldellis JK, Triantafyllou P, Stinis P. Critical evaluation of Wind Turbines' analytical wake models. Renew Sustain Energy Rev 2021;144:110991.

[43] Zhang J, Zhao X. A novel dynamic wind farm wake model based on deep learning. Appl Energy 2020;277:115552.

[44] Jiang P, Liu Z, Niu X, Zhang L. A combined forecasting system based on statistical method, artificial neural networks, and deep learning methods for short-term wind speed forecasting. Energy 2021;217:119361.

[45] Zhang J, Zhao X. Wind farm wake modeling based on deep convolutional conditional generative adversarial network. Energy 2022;238:121747.

[46] Karasu S, Altan A, Saraç Z, Hacioğlu R. Estimation of fast varied wind speed based on NARX neural network by using curve fitting. Int J Energy Appl Technol 2017;4(3):137–46.

[47] Karasu S, Altan A. Recognition model for solar radiation time series based on random forest with feature selection approach. In: 2019 11th international conference on electrical and electronics engineering. IEEE; 2019, p. 8–11.

[48] Altan A, Karasu S, Zio E. A new hybrid model for wind speed forecasting combining long short-term memory neural network, decomposition methods and grey wolf optimizer. Appl Soft Comput 2021;100:106996.

[49] Sun S, Liu Y, Li Q, Wang T, Chu F. Short-term multi-step wind power forecasting based on spatio-temporal correlations and transformer neural networks. Energy Convers Manage 2023;283:116916.

[50] Nascimento EGS, de Melo TA, Moreira DM. A transformer-based deep neural network with wavelet transform for forecasting wind speed and wind energy. Energy 2023;278:127678.

[51] Liu L, Liu J, Ye Y, Liu H, Chen K, Li D, et al. Ultra-short-term wind power forecasting based on deep Bayesian model with uncertainty. Renew Energy 2023;205:598–607.

[52] Xing Z, He Y. Multi-modal multi-step wind power forecasting based on stacking deep learning model. Renew Energy 2023:118991.

[53] ZXLidars Product Guide. 2021, https://www.zxlidars.com.

[54] Martínez-Tossas LA, Churchfield MJ, Leonardi S. Large eddy simulations of the flow past wind turbines: actuator line and disk modeling. Wind Energy 2015;18(6):1047–60.

[55] Boersma S, Doekemeijer B, Vali M, Meyers J, van Wingerden J-W. A control-oriented dynamic wind farm model: WFSim. Wind Energy Sci 2018;3(1):75–95.

[56] Raissi M, Perdikaris P, Karniadakis GE. Physics-informed neural networks: A deep learning framework for solving forward and inverse problems involving nonlinear partial differential equations. J Comput Phys 2019;378:686–707.

[57] Karniadakis GE, Kevrekidis IG, Lu L, Perdikaris P, Wang S, Yang L. Physics-informed machine learning. Nat Rev Phys 2021;3(6):422–40.

[58] Raissi M, Yazdani A, Karniadakis GE. Hidden fluid mechanics: Learning velocity and pressure fields from flow visualizations. Science 2020;367(6481):1026–30.

[59] Cai S, Li H, Zheng F, Kong F, Dao M, Karniadakis GE, et al. Artificial intelligence velocimetry and microaneurysm-on-a-chip for three-dimensional analysis of blood flow in physiology and disease. Proc Natl Acad Sci 2021;118(13).

[60] Cavanagh H, Mosbach A, Scalliet G, Lind R, Endres RG. Physics-informed deep learning characterizes morphodynamics of Asian soybean rust disease. Nat Commun 2021;12(1):1–9.

[61] Zhang J, Zhao X. Spatiotemporal wind field prediction based on physics-informed deep learning and LIDAR measurements. Appl Energy 2021;288:116641.

[62] Zhang J, Zhao X. Three-dimensional spatiotemporal wind field reconstruction based on physics-informed deep learning. Appl Energy 2021;300:117390.

[63] Churchfield M, Lee S. NWTC design codes-SOWFA. 2012, URL http://wind.nrel.gov/designcodes/simulators/SOWFA.

[64] Churchfield MJ, Lee S, Michalakes J, Moriarty PJ. A numerical study of the effects of atmospheric and wake turbulence on wind turbine dynamics. J Turbulence 2012;(13):N14.

[65] Doubrawa P, Churchfield MJ, Godvik M, Sirnivas S. Load response of a floating wind turbine to turbulent atmospheric flow. Appl Energy 2019;242:1588–99.

[66] Jiménez Á, Crespo A, Migoya E. Application of a LES technique to characterize the wake deflection of a wind turbine in yaw. Wind energy 2010;13(6):559–72.

[67] Dou B, Guala M, Lei L, Zeng P. Experimental investigation of the performance and wake effect of a small-scale wind turbine in a wind tunnel. Energy 2019;166:819–33.

[68] Munters W, Meyers J. Dynamic strategies for yaw and induction control of wind farms based on large-eddy simulation and optimization. Energies 2018;11(1):177.

[69] Kheirabadi AC, Nagamune R. A quantitative review of wind farm control with the objective of wind farm power maximization. J Wind Eng Ind Aerodyn 2019;192:45–73.

[70] Kingma DP, Ba J. Adam: A method for stochastic optimization. 2014, arXiv preprint arXiv:1412.6980.

[71] Churchfield M, Lee S, Moriarty P. Overview of the simulator for wind farm application (SOWFA). 2012, National Renewable Energy Laboratory.

[72] Yang X, Sotiropoulos F. A review on the meandering of wind turbine wakes. Energies 2019;12(24):4725.

[73] Wise AS, Bachynski EE. Wake meandering effects on floating wind turbines. Wind Energy 2020;23(5):1266–85.

[74] Fleming P, Annoni J, Shah JJ, Wang L, Ananthan S, Zhang Z, et al. Field test of wake steering at an offshore wind farm. Wind Energy Sci 2017;2(1):229–39.

[75] Fleming P, King J, Dykes K, Simley E, Roadman J, Scholbrock A, et al. Initial results from a field campaign of wake steering applied at a commercial wind farm–part 1. Wind Energy Sci 2019;4(2):273–85.

[76] Doekemeijer BM, Kern S, Maturu S, Kanev S, Salbert B, Schreiber J, et al. Field experiment for open-loop yaw-based wake steering at a commercial onshore wind farm in Italy. Wind Energy Sci 2021;6(1):159–76.